

Measured Spin-Orbit Alignment of Ultra-Short Period Super-Earth 55 Cancri e

LILY L. ZHAO,¹ VEDAD KUNOVAC,² JOHN M. BREWER,³ JOE LLAMA,² SARAH C. MILLHOLLAND,⁴ CHRISTINA HEDGES,^{5,6}
 ANDREW E. SZYMKOWIAK,^{7,8} RACHAEL M. ROETTENBACHER,⁹ SAMUEL H. C. CABOT,⁷ SAM A. WEISS,⁷
 DEBRA A. FISCHER,⁷

¹Center for Computational Astrophysics, Flatiron Institute, Simons Foundation, 162 Fifth Avenue, New York, NY 10010, USA

²Lowell Observatory, 1400 W. Mars Hill Rd., Flagstaff, AZ 86001, USA

³Dept. of Physics & Astronomy, San Francisco State University, 1600 Holloway Ave., San Francisco, CA 94132, USA

⁴MIT Kavli Institute for Astrophysics and Space Research, Massachusetts Institute of Technology, Cambridge, MA 02139, USA

⁵University of Maryland, Baltimore County, 1000 Hilltop Cir, Baltimore, MD 21250, USA

⁶NASA Goddard Space Flight Center, 8800 Greenbelt Rd, Greenbelt, MD 20771, USA

⁷Department of Astronomy, Yale University, 52 Hillhouse Ave., New Haven, CT 06511, USA

⁸Department of Physics, Yale University, 217 Prospect St, New Haven, CT 06511, USA

⁹Department of Astronomy, University of Michigan, 1085 S. University Ave., Ann Arbor, MI 48109, USA

ABSTRACT

A planet’s orbital alignment places important constraints on how a planet formed and consequently evolved. The dominant formation pathway of ultra-short period planets ($P < 1$ day) is particularly mysterious as such planets most likely formed further out, and it is not well understood what drove their migration inwards to their current positions. Measuring the orbital alignment is difficult for smaller super-Earth/sub-Neptune planets, which give rise to smaller amplitude signals. Here we present radial velocities across two transits of 55 Cancri e, an ultra-short period Super-Earth, observed with the Extreme Precision Spectrograph (EXPRES). Using the classical Rossiter-McLaughlin (RM) method, we measure 55 Cnc e’s sky-projected stellar spin-orbit alignment (i.e., the projected angle between the planet’s orbital axis and its host star’s spin axis) to be $\lambda = 10_{-20}^{+17}$ ^o with an unprojected angle of $\psi = 23_{-12}^{+14}$ ^o. The best-fit RM model to the EXPRES data has a radial velocity semi-amplitude of just $0.41_{-0.10}^{+0.09}$ m s⁻¹. The spin-orbit alignment of 55 Cnc e favors dynamically gentle migration theories for ultra-short period planets, namely tidal dissipation through low-eccentricity planet-planet interactions and/or planetary obliquity tides.

1. INTRODUCTION

55 Cancri hosts five known exoplanets with minimum mass estimates ranging from approximately $8 M_{\oplus}$ to $3 M_{\text{Jup}}$ and periods less than one day to nearly 20 years (Butler et al. 1997; Marcy et al. 2002; McArthur et al. 2004; Fischer et al. 2008). Of particular interest has been 55 Cnc e, one of the most massive known ultra-short-period planets (USP) and the only planet around 55 Cnc found to transit (Winn et al. 2011; Demory et al. 2011). It has an orbital period of $0.7365474_{-1.4E-6}^{+1.3E-6}$ days, a mass of $7.99 \pm 0.33 M_{\oplus}$, and a radius of $1.853_{-0.027}^{+0.026}$ (Dawson & Fabrycky 2010; Bourrier et al. 2018). A precise measure of 55 Cnc e’s stellar spin-orbit alignment—the angle between the host star’s spin axis and the planet’s orbit normal—will shed light on the formation and evolution of USPs, especially in the case of compact, multi-planet systems.

It has been shown that USPs form a statistically distinct population of planets (Steffen & Coughlin 2016) that tend to be misaligned with other planetary orbits in their system (Dai et al. 2018). This suggests that USPs experience a unique migration pathway that brings them close in to their host stars. This inward migration is most likely driven by dissipation due to star-planet tidal interactions that result from either non-zero eccentricities (Petrovich et al. 2019; Pu & Lai 2019) or planetary spin-axis tilts (Millholland & Spalding 2020).

The stellar spin-orbit alignment of a transiting planet can be measured by obtaining spectroscopic observations during the planet's transit. Commonly called the Rossiter-McLaughlin (RM) effect (Triaud 2018; Albrecht et al. 2022), radial velocity (RV) deviations as a planet transits a rotating star reveal whether the planet is transiting across the blue-shifted half of the star that rotates towards the observer or the red-shifted half of the star that rotates away. Capturing the resultant net red-/blue-shift reveals the orientation of the planet's orbital normal vector with respect to its host star's spin vector, i.e., the sky-projected stellar spin-orbit alignment or the stellar obliquity.

Previous attempts to measure the RM effect for 55 Cnc e have produced mixed results. Using data from the High Accuracy Radial velocity Planet Searcher for the Northern hemisphere (HARPS-N), Bourrier & Hébrard (2014) reported a sky-projected obliquity of $\lambda = 72_{-12}^{+13}$. However, the best fit model from that analysis also returned a stellar projected rotational velocity of $v \sin i_{\star} = 3.3 \pm 0.9$ km s $^{-1}$, which is not consistent with the $v \sin i_{\star}$ measured by other studies (Bourrier et al. 2018). A separate observing campaign also using HARPS-N data reported a non-detection and rule out an RM signal with an amplitude greater than ~ 35 cm s $^{-1}$ (López-Morales et al. 2014).

Here we present a 41_{-10}^{+9} cm s $^{-1}$ amplitude RM detection of 55 Cnc e using observations from the Extreme Precision Spectrograph (EXPRES). The arrival of ultra-stabilized spectrographs, including EXPRES and ESPRESSO among others, have made sub-meter-per-second RV precision possible (Pepe et al. 2013; Jurgenson et al. 2016). This measurement is the smallest amplitude classic RM detection to date. Precision RV measurements from spectrographs like EXPRES will be able to detect lower-amplitude RM effects that have previously been missed in the regime of small planets or slowly rotating stars.

2. RESULTS

We use two sectors of TESS photometry to fit for the transit parameters of 55 Cnc e, which are then used to constrain the RM model. We use RV measurements from EXPRES to detect and fit for the RM effect during two 55 Cnc e transits observed on Jan. 31 2022 and Apr. 6, 2022. The EXPRES spectra were also used to derive stellar properties for 55 Cnc using Spectroscopy Made Easy (SME) (Brewer et al. 2016; Piskunov & Valenti 2017).

The EXPRES RVs and RM fits are shown in Figure 1. The best-fit RM models for each individual night as well as the combined data are plotted over the EXPRES data in yellow with darker and lighter shading showing the 50th and 90th percentile of the posterior distribution, respectively. The full posterior distribution was sampled using a Markov chain Monte Carlo (MCMC).

With the combined fit using both nights of observations, we find that 55 Cnc e has a sky-projected stellar obliquity of $\lambda = 10_{-20}^{+17}$. By incorporating the rotation period of 55 Cnc (Bourrier et al. 2018) we derive an un-projected stellar

Table 1. 55 Cnc e Fit Parameters

Parameter	Symbol	Value	Unit	Prior
Transit Fit				
Planet/star radii ratio	R_p/R_{\star}	$0.018016_{-0.000077}^{+0.000085}$		LogNormal($-8, 10$)
Radius	R_p	$1.856_{-0.025}^{+0.024}$	R_{\oplus}	—
Orbital period	P	0.7365430 ± 0.0000014	days	Normal($0.736546, 1$)
Transit epoch	T_0	$2459511.487987_{-0.000075}^{+0.000071}$	BJD _{TDB}	Normal($2459511.48778, 1$)
Impact parameter	b	$0.373_{-0.032}^{+0.027}$	R_{\star}	Uniform($0, 1$)
Orbital inclination	i	$83.9_{-0.5}^{+0.6}$	deg	—
Orbital separation	a/R_{\star}	$3.516_{-0.041}^{+0.042}$		—
Transit duration	T_{14}	$1.5439_{-0.0026}^{+0.0027}$	hours	—
Limb-darkening	u_1	0.4823 ± 0.0017		Normal($0.4824, 0.0017$)
	u_2	$0.1276_{-0.0041}^{+0.0037}$		Normal($0.1280, 0.0038$)
RM Fit				
<i>Fitted parameters</i>				
Sky-projected obliquity	λ	10_{-20}^{+17}	deg	Uniform($-180^{\circ}, 180^{\circ}$)
Projected rotational velocity	$v \sin i_{\star}$	$2.00_{-0.47}^{+0.43}$	km s $^{-1}$	Uniform($0, 18$)
Net convective blueshift velocity	V_{CB}	-157_{-94}^{+86}	m s $^{-1}$	Uniform($-1000, 0$), Normal($-150, 100$)
<i>Derived parameters</i>				
RM semi-amplitude	K_{RM}	$0.41_{-0.10}^{+0.09}$	m s $^{-1}$	
Stellar inclination	i_{\star}	75_{-18}^{+11}	deg	
Obliquity	ψ	23_{-12}^{+15}	deg	

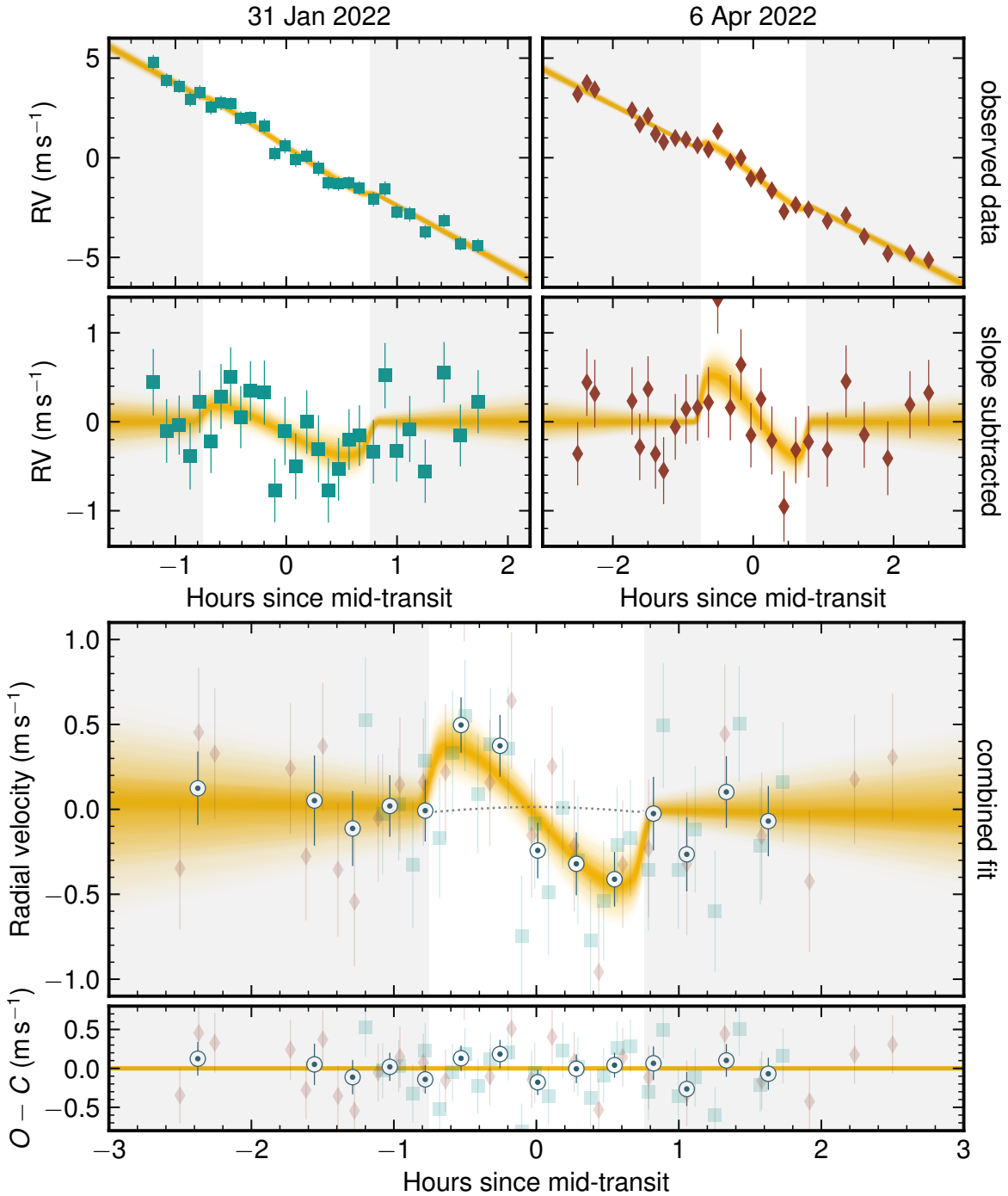


Figure 1. Rossiter-McLaughlin model fit to two nights of EXPRES RV data. Data from Jan. 31, 2022 are shown as green squares, Apr. 6, 2022 as red diamonds. The RV value (indicated by each marker) represents the best-fit Doppler shift produced by the EXPRES chunk-by-chunk, forward modeling pipeline with error bars spanning the corresponding $1-\sigma$ errors (see (Petersburg et al. 2020) for more information on the EXPRES pipeline). RM models are shown as yellow curves. Shaded yellow regions span 50th to 99th percentile of the posterior sampled by the MCMC. The white highlighted area spans the transit duration of 55 Cnc e. Panels a-d show each of the two nights of observations individually. Panels a and b show the original RVs along with the full model fit for each night. Panels c and d show the RVs and model fit with the best fit linear slope removed. Panel e shows the combined fit to both nights of data and the residuals to the best fit. White circular points represent both nights of data binned by phase with points every 0.015 phase units (~ 15.9 minutes) to help guide the eye. Phase binned points are calculated as the average of all data points within the phase bin weighted by their errors, σ_i , with associated errors given by $\sqrt{\frac{1}{\sum 1/\sigma_i^2}}$. The dotted gray line represents the center-to-limb convective blueshift contribution to the RVs, which has a semi-amplitude of 1.3 cm s^{-1} .

obliquity of $\psi = 23^{+14}_{-12}^\circ$. We therefore find that 55 Cnc e's orbit normal is close to aligned with its host star's rotation axis. The best-fit transit and RM parameters are given in Table 1 along with the priors used in the fitting. Other nuisance parameters needed for each fit as well as the results of the fits to each individual night are given in Table 2 and described more fully in Section 4 below. The measured stellar spin-orbit alignment of 55 Cnc e is graphically represented in Figure 2.

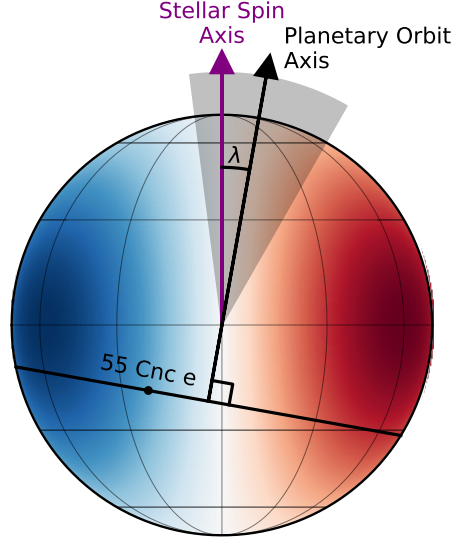


Figure 2. A visual representation of the sky-projected alignment between 55 Cnc e's stellar spin axis (purple) and planetary orbit axis (mean shown in black). The apparent Doppler shift of the star's surface that arises from its rotation is shown in shades of blue to red, which correspond to the degree to which the stellar surface appears blue- or red-shifted. Lighter shading corresponds to smaller Doppler shift. The star is shown with an inclination $i_\star = 90^\circ$, which is consistent with the wide constraints on our estimate of i_\star . The $1-\sigma$ confidence level for 55 Cnc e's orbit axis is shown by the gray shading. The transit trajectory is shown as a black band. The size of the planet is to scale with the size of the star.

3. DISCUSSION

We recover a statistically significant detection of the RM effect for 55 Cnc e using EXPRES data with a false alarm probability of 0.3%. The amplitude of the measured signal, $K_{\text{RM}} = 0.41^{+0.09}_{-0.10} \text{ m s}^{-1}$, is the smallest classically recovered RM measurement to date. Two other super-Earth systems have similar expected RM amplitudes, but could only be detected using stellar line profile analysis (Kunovac Hodžić et al. 2021; Bourrier et al. 2021).

This result clarifies previous measurements of 55 Cnc e's stellar spin-orbit alignment, which gave contradictory results (Bourrier & Hébrard 2014; López-Morales et al. 2014). Bourrier & Hébrard (2014) previously reported best fit RM values of $\lambda = 72^{+13}_{-12}^\circ$ and $v \sin i_\star = 3.3 \pm 0.9 \text{ km s}^{-1}$. This $v \sin i_\star$ value is $\sim 1.8\sigma$ greater than the literature value derived from stellar line broadening, which report the $v \sin i_\star$ as $1.7 \pm 0.5 \text{ km s}^{-1}$ (Brewer et al. 2016). The RM fit presented here returns a best-fit $v \sin i_\star$ of $2.00^{+0.43}_{-0.47} \text{ km s}^{-1}$, which is within 1σ -agreement of the literature value. Our RM fit additionally agrees with the independent SME line broadening analysis, which returned a $v \sin i_\star$ of $1.94 \pm 0.50 \text{ km s}^{-1}$. These $v \sin i_\star$ values are in some tension with the rotational velocity calculated using the stellar radius and rotation period ($v = \frac{2\pi R_\star}{P_\star} = 1.23 \pm 0.01 \text{ km s}^{-1}$) by $\sim 1.5\sigma$. However, the agreement between the two methods used here as well as agreement with literature values (Valenti & Fischer 2005; Brewer et al. 2016) suggests this is due to uncertainties in the quoted rotation period possibly due to differential rotation or spots.

The EXPRES data used in this analysis have a consistent and often higher SNR as well as lower uncertainties than the RV measurements previously used. All EXPRES observations were integrated until they reached a constant SNR of 225 at 550 nm; this consistency in SNR allowed for more stable final RVs with similar error properties. Though it

Table 2. TESS and EXPRES Fitted Nuisance Parameters

Parameter	Symbol	Value	Unit	Prior
TESS Fit				
<i>Sector 44</i>				
GP amplitude	σ_{GP}	$0.234^{+0.028}_{-0.022}$	ppt	LogNormal($-8, 10$)
GP timescale	τ_{GP}	$1.086^{+0.135}_{-0.105}$	day	LogNormal($2, 10$)
Mean flux	f	0.045 ± 0.035	ppt	Normal($0, 10$)
White noise	σ	0.0980 ± 0.0012	ppt	LogNormal($-16, 10$)
<i>Sector 46</i>				
GP amplitude	σ_{GP}	$0.112^{+0.016}_{-0.013}$	ppt	LogNormal($-8, 10$)
GP timescale	τ_{GP}	$2.22^{+0.32}_{-0.23}$	day	LogNormal($2, 10$)
Mean flux	f	$0.018^{+0.022}_{-0.021}$	ppt	Normal($0, 10$)
White noise	σ	$0.0965^{+0.0011}_{-0.0012}$	ppt	LogNormal($-16, 10$)
EXPRES Fit				
<i>Jan. 31 2022</i>				
Sky-projected obliquity	λ	34^{+24}_{-26}	deg	Uniform($-180^\circ, 180^\circ$)
Projected rotational velocity	$v \sin i_\star$	$1.74^{+0.62}_{-0.68}$	km s^{-1}	Uniform($0, 18$)
Intercept	y_0	$0.646^{+0.034}_{-0.033}$	m s^{-1}	—
Slope	m	$-72.4^{+2.0}_{-2.1}$	$\text{m s}^{-1} \text{ day}^{-1}$	Uniform($-150, -50$)
<i>Apr. 6 2022</i>				
Sky-projected obliquity	λ	-19^{+30}_{-20}	deg	Uniform($-180^\circ, 180^\circ$)
Projected rotational velocity	$v \sin i_\star$	$2.36^{+0.59}_{-0.65}$	km s^{-1}	Uniform($0, 18$)
Intercept	y_0	$-0.952^{+0.023}_{-0.022}$	m s^{-1}	—
Slope	m	$-43.1^{+1.4}_{-1.3}$	$\text{m s}^{-1} \text{ day}^{-1}$	Uniform($-150, -5$)

Note: The given uncertainties represent each measurement's 68% credible interval.

is difficult to compare SNR between different spectrographs given each instrument's unique throughput response as a function of wavelength, we report that López-Morales et al. (2014) used observations that ranged in SNR between 100 and 275 with a median SNR of 165 at 624 nm. Bourrier & Hébrard (2014) give a median SNR across all nights of 144 at 527 nm with the median SNR within a night ranging from 92 to 354. The HARPS-N RVs previously used have a median error of about 80 cm s^{-1} and were calibrated using either a ThAr lamp or a Fabry-Pérot while the EXPRES RVs have a median error of 38 cm s^{-1} and are calibrated using a laser frequency comb. The EXPRES observations are more stable, have smaller RV uncertainties, and return a best-fit RM model more aligned with literature values than previous attempts at measuring 55 Cnc e's stellar spin-orbit alignment.

With this robust measurement using EXPRES data, we can place constraints on the different proposed dynamical histories for the 55 Cnc system. Studies have suggested that due to 55 Cnc's distant stellar companion, one would expect all the planets around 55 Cnc to precess as a rigid plane around the host star, resulting in all planets sharing a common planetary orbit axis that is misaligned with respect to the host star's spin axis (Kaib et al. 2011). Other simulations propose that secular resonances between 55 Cnc e and the other planets in the system led to excitation of 55 Cnc e's eccentricity and inclination, causing 55 Cnc e's orbital axis to be misaligned with the other planets' orbital axes as well as the host star's spin axis (Hansen & Zink 2015). Analysis using the system's precession frequencies (Boué & Fabrycky 2014a), on the other hand, finds that one would expect to find 55 Cnc e's orbital axis close to aligned with its host star's spin axis (Boué & Fabrycky 2014b), which is what our measurement shows.

Various theories for the migration pathways of USPs differ in terms of the predicted spin-orbit alignments. Secular planet-planet interactions have been shown to give rise to tidal dissipation inside the planets and can operate under both a high-eccentricity and low-eccentricity mode. The high-eccentricity mode leads to excitation of planetary eccentricities and inclinations through secular chaos, resulting in generally misaligned systems with large stellar spin-orbit alignment angles and USPs whose orbits have decayed to close-in, circular orbits (Petrovich et al. 2019). Planet-planet interactions can also lead to the inward migration of planets even in the case of modest eccentricities (Pu & Lai 2019). This mechanism is less chaotic and likely results in USP orbits that are aligned to within a few tens of degrees.

Planetary obliquity tides have also been proposed as a source for tidal dissipation of USPs (Millholland & Spalding 2020). Here, planetary obliquity is used to refer to the angle between the planet's spin axis and the planet's orbital plane (as opposed to the stellar obliquity). Planetary-obliquity-driven tidal dissipation has no requirements on initial

planet eccentricities. This mechanism predicts that a planet's orbit normal will become closer to aligned with the host star's spin axis as it migrates inwards, but may be misaligned with the orbit normals of other planets in the system.

The close alignment of 55 Cnc e's orbit normal with its host star's stellar axis preliminarily favors the low eccentricity (Pu & Lai 2019) and planetary obliquity (Millholland & Spalding 2020) tide models. It is of particular interest that 55 Cnc e is the only planet of the five known planets around 55 Cnc that transits. This suggests that though 55 Cnc e's orbit normal is aligned with the spin axis of its host star, it is possibly misaligned from those of the other planets. This is expected from the planetary obliquity tides model if there existed some primordial misalignment of the stellar obliquity, for example due to 55 Cnc's distant binary companion (Kaib et al. 2011).

In the scenario with an initial misalignment, 55 Cnc e may have formed out of the protoplanetary disk with an orbital plane aligned with the outer planets, but as it migrated inward, 55 Cnc e became more influenced by the gravitational quadrupole moment of the star, causing it to become more aligned with the stellar equatorial plane as it settled into its final, short-period orbit (Millholland & Spalding 2020). The final state of 55 Cnc e would therefore be misaligned with the orbital planes of the outer, non-transiting planets, but aligned with the host star's spin equatorial plane as measured.

This type of system architecture for USPs is supported by previous studies. Kepler USPs in multi-planet systems have been found to have larger mutual inclinations with the other outer planets (Dai et al. 2018). Recent analysis of HD 3167 b, an ultra-short period Super-Earth ($P = 0.959641^{+1.1E-5}_{-1.2E-5}$; $M_p = 5.02 \pm 0.38 M_{\oplus}$), and HD 3167 c, a Sub-Neptune on a 30 day period, returned a similar system architecture (Christiansen et al. 2017; Bourrier et al. 2021). The inner USP, HD 3167 b, was found to have an orbit normal closely aligned with its host star's spin axis ($\psi = 29.5^{+7.2}_{-9.4}^{\circ}$) while the further out planet, HD 3167 c, has an orbit nearly perpendicular to the orbit of HD 3167 b ($\psi = 107.7^{+5.1}_{-4.9}^{\circ}$). We find that 55 Cnc similarly has a USP, 55 Cnc e, with an orbit aligned with the stellar equatorial plane though the alignment of the outer planets are unclear since they do not transit.

The close alignment of the ultra-short period, Super-Earth 55 Cnc e's orbit normal with its host star's spin axis places constraints on theories for how USPs migrate to their present day positions and how they interact with other planets in compact multi-planet systems. This measurement additionally gives clues as to why none of the other known planets around 55 Cnc transit and the possible role of 55 Cnc's distant stellar companion. This small-amplitude RM measurement of a Super-Earth is only now achievable because of new, ultra-stabilized spectrographs capable of delivering sub-meter-per-second precision. More spin-orbit alignment measurements of USPs will help us to understand this unique population of planets and the nature of the planetary tidal dissipation that cause them to migrate so close-in to their host stars.

4. METHODS

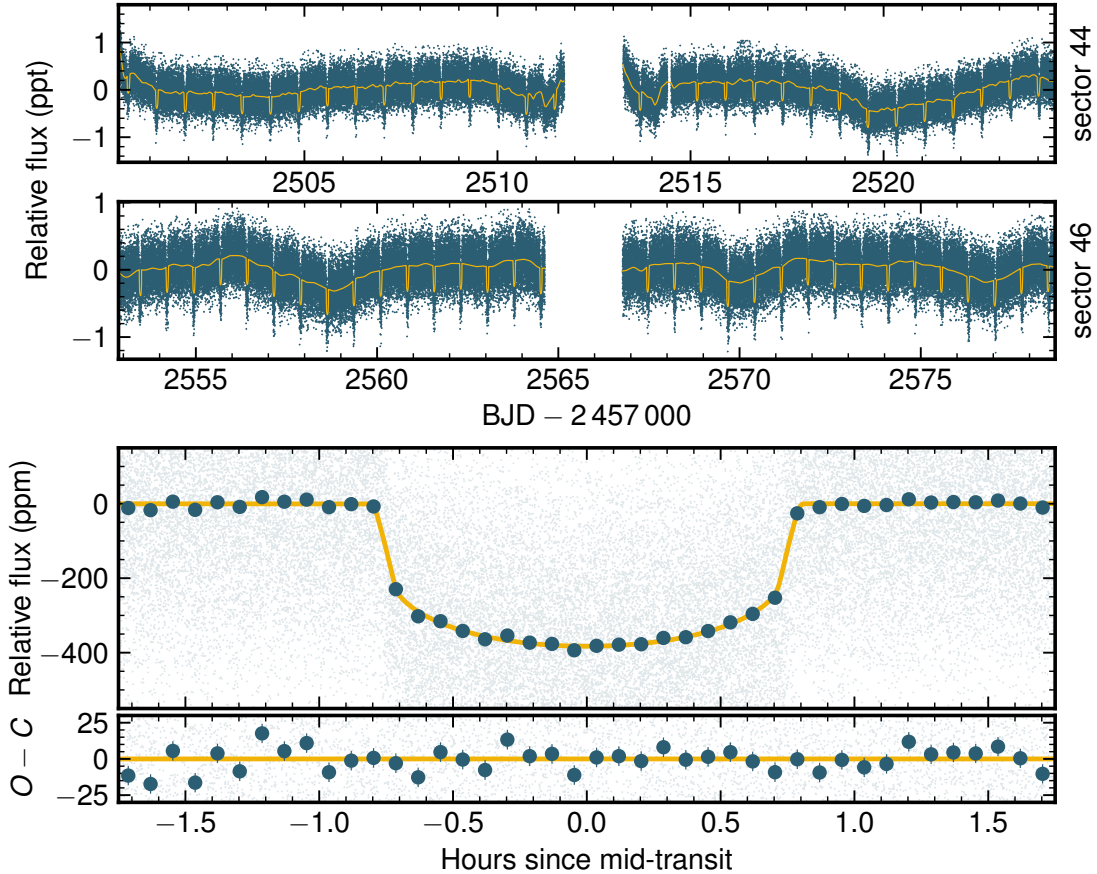
4.1. Photometric Data and Transit Fit

TESS observed 55 Cnc at a two-minute cadence during Sector 21 (Jan. 21 - Feb. 18 2020) and a 20-s cadence during Sector 44 (Oct. 12 - Nov. 5 2021) and Sector 46 (Dec. 3-30 2021). We use the publicly available light curves that have been detrended of common instrumental systematics (Jenkins 2016). We found evidence of high-frequency correlated noise throughout the first sector (Sector 21) of observations, and therefore use only the later two sectors (i.e., Sectors 44 and 46) with 20-s exposure times. In total, we used 199,838 TESS cadences of 55 Cnc.

Both sectors of TESS data are fit for simultaneously with a Hamiltonian MCMC implemented using `exoplanet`, PyMC3, and `Theano` (Foreman-Mackey et al. 2020; Salvatier et al. 2016; Theano Development Team 2016). The fit is parameterized using the stellar mass and radius rather than just the stellar density since the planet has a low eccentricity and there exists direct interferometric constraints on the stellar radius of 55 Cnc (von Braun et al. 2011). The Gaussian priors for the stellar mass and radius are given in Supplementary Table 1. We additionally fit for the orbital period, P , transit mid-time, T_0 , planet-to-star radius ratio, R_p/R_{\star} , and impact parameter, b . Each sector is also fit to an independent GP model using a Matérn-3/2 kernel parametrized by an amplitude σ_{GP} and a timescale τ_{GP} to account for any background variations in the light curve (Foreman-Mackey et al. 2017; Foreman-Mackey 2018). The model also includes a mean flux and a white noise term to inflate the photon noise uncertainties from TESS.

The model included quadratic limb darkening, with coefficients determined using the LDTk code package (Parviainen & Aigrain 2015). This code uses the PHOENIX stellar atmosphere models (Husser et al. 2013) to generate observed disk intensities based on the TESS bandpass and input stellar parameters T_{eff} , Fe/H, and $\log g$ that were obtained from spectroscopic analysis (Supplementary Table 1). The limb-darkening coefficients were fit for as part of the model and were constrained using Gaussian priors, though the uncertainties were inflated by a factor of five to account for the

uncertainties in the stellar model. We ran two independent chains for 1500 tuning steps and 1000 production steps. We verified that convergence was reached by making sure the \hat{R} metric, as defined in Gelman et al. (2003), was below a conservative 1.001 threshold. We additionally ensured that the effective number of samples per parameter was >200 . The TESS data and best-fit transit model is shown in Supplementary Figure 1. The resultant transit fit parameters, which agree with literature values (Bourrier et al. 2018; Demory et al. 2016; Kipping & Jansen 2020), are given in Table 1 with the GP parameters given in Table 2.



Supplementary Figure 1. Fit to two sectors of TESS photometry. Panels a and b show the full time series of 20-second exposures in blue with the best-fit transit model over plotted in yellow. Panel c shows the phase-folded light curve with the GP model accounting for background variations removed. In panel c, each individual exposure is shown as a light blue point. Dark blue points are phase binned into 5-minute averages and are shown as a visual aid. Phase binned points are calculated as the average of all data points within the phase bin weighted by their errors, σ_i , with associated errors given by $\sqrt{\frac{1}{\sum 1/\sigma_i^2}}$. Phase-binned residuals to the transit model are shown in the bottom most panel.

4.2. Spectroscopic Data

EXPRES observed 55 Cnc e during transit on Jan. 31, 2022 (28 observations) and Apr. 6, 2022 (27 observations). EXPRES is a stabilized, next-generation, optical (390 – 780 nm) spectrograph with a high median resolving power of $R \sim 137,000$ (Jurgenson et al. 2016) mounted on the 4.3-m Lowell Discovery Telescope (LDT) (Levine et al. 2012). It has a measured instrument stability of $3\text{--}7\text{ cm s}^{-1}$ and returns an intra-night scatter of $10\text{--}40\text{ cm s}^{-1}$ on-sky for select quiet stars (Blackman et al. 2020; Zhao et al. 2022).

EXPRES observations were terminated after they reached an SNR of 225, which corresponds to a resultant analytical RV error of approximately 35 cm s^{-1} (Petersburg et al. 2020). Most observations took between 4 and 9 minutes. The last five observations on Apr. 6, which fall after the transit, required longer exposure times of 15–17 minutes to reach the target SNR as the weather quickly degraded. RVs are derived using a template-matching, chunk-by-chunk technique. These RV measurements are given in Supplementary Table 2.

4.3. 55 Cnc Stellar Properties

We also use the EXPRES spectra to derive stellar properties of 55 Cnc (Brewer et al. 2016). The analysis uses the forward modeling tool, Spectroscopy Made Easy (SME) (Piskunov & Valenti 2017), to fit both the global stellar properties and individual abundances of 15 elements using more than 7000 atomic and molecular lines over ~ 350 Å of spectrum. The method first fits for T_{eff} , $\log g$, rotational broadening, and a scaled solar abundance pattern [M/H], with only calcium, silicon, and titanium allowed to vary independently. The temperature of this model is perturbed ± 100 K, and the parameters are re-derived. The global parameters are then fixed to those found while the abundances of 15 elements (C, N, O, Na, Mg, Al, Si, Ca, Ti, V, Cr, Mn, Fe, Ni, and Y) are allowed to vary. These steps are then repeated, this time starting with the newly-derived abundance pattern. Finally, a temperature and gravity dependent macroturbulence is assigned and we solve for $v \sin i_*$ with all other parameters fixed.

In total, 290 EXPRES 55 Cnc spectra were analyzed in this way; the χ^2 weighted averages adopted for the parameters can be found in Supplementary Table 1. The distribution of returned model parameters gives us a measure of the model fit for this star but does not take into account uncertainties in the model itself. The standard deviations in returned T_{eff} , $\log g$, and $v \sin i_*$ were 5 K, 0.015 dex, and 0.05 km/s respectively. We therefore adopt the larger uncertainties that take into account model uncertainties across a range of stellar parameters (Brewer et al. 2016).

Supplementary Table 1. 55 Cnc Stellar Parameters Derived using SME

Parameter	Symbol	Value	Unit	Reference
Radius	R_*	0.943 ± 0.010	R_{\odot}	von Braun et al. 2011
Mass	M_*	0.905 ± 0.015	M_{\odot}	von Braun et al. 2011
Rotation Period	P_*	38.8 ± 0.05	days	Bourrier et al. 2018
This Work				
Projected rotational velocity	$v \sin i_*$	1.94 ± 0.50	km s $^{-1}$	
Effective temperature	T_{eff}	5272 ± 24	K	
Surface gravity	$\log g$	4.38 ± 0.05	m s $^{-2}$	
Metallicity	[Fe/H]	0.37 ± 0.02		

4.4. Rossiter-McLaughlin Fit

We model the Rossiter-McLaughlin signal in the EXPRES radial velocity data using `ellc` (Ohta et al. 2005; Maxted 2016). The `emcee` ensemble sampler is used to perform MCMC sampling to find the range of parameters compatible with the data (Foreman-Mackey et al. 2013). In the MCMC sampling, we allow the projected stellar rotation, $v \sin i_*$, and sky-projected stellar obliquity, λ , to vary uniformly in the range 0-20 km s $^{-1}$ and -180 to 180 degrees, respectively. By using uniform priors for $v \sin i_*$ rather than priors based on the value determined by SME, we are able to get independent measures of $v \sin i_*$ from both SME and the RM fit.

For each transit, our model includes a white noise term to inflate the photon noise uncertainty as well as a linear model with parameters y_0 (intercept) and m (slope) to account for the stellar reflex motion due to the orbiting planets. The slope is a free parameter that is fit to the out-of-transit data at every step in the MCMC. The intercept is then determined from a weighted average of the out-of-transit residuals after subtracting the slope.

Supplementary Table 2. Chunk-by-Chunk RVs

Time [BMJD _{UTC}]	RV [m s $^{-1}$]	Err. [m s $^{-1}$]
59610.371	87.665	0.345
59610.376	86.737	0.337
59610.381	86.493	0.3
:	:	:

NOTE—A stub of this table is provided here for reference; the full RV data set is available online.

The transit also gives rise to a second radial velocity anomaly due to turbulent convective motion on the surface of the star (Cegla et al. 2016). We include a model for the convective blueshift variation (Shporer & Brown 2011) and assume a net convective blueshift centered on $V_{\text{CB}} = -150 \text{ m s}^{-1}$ (Meunier et al. 2017; Liebing et al. 2021) with a standard deviation of 100 m s^{-1} . The contribution of the convective blueshift model has a semi-amplitude of 1.3 cm s^{-1} and is shown as a gray dotted line in Figure 1.

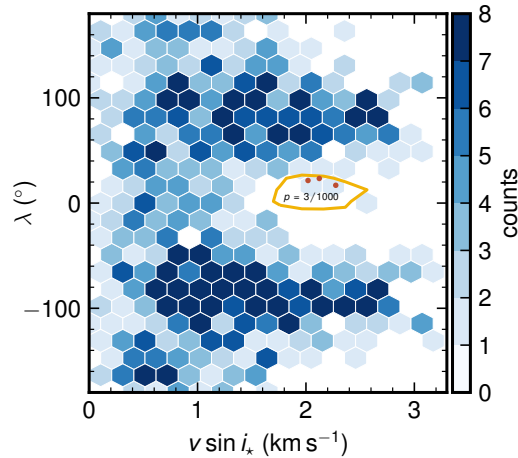
The orbital period P , transit time t_0 , scaled separation a/R_\star , radius ratio r/R_\star , and orbital inclination i are updated in every step of the MCMC by sampling from a multivariate normal distribution, the mean and covariance properties of which are determined from the posterior distribution obtained from the TESS analysis. This effectively places Gaussian priors on the transit parameters, but also takes into account their covariance.

We ran an ensemble of 300 emcee “walkers” for 2000 steps each, discarded 750 samples as a burn-in, thinned the chains by the autocorrelation length, and finally merged the chains together to obtain 3300 independent samples. The median values and 68% confidence interval for the fit for RM parameters are reported in Table 1. The range of models compatible with the data to the 99th percentile are illustrated in Figure 1 by the yellow shading.

The Rossiter-McLaughlin effect is only able to measure the sky-projection of the stellar obliquity, λ . The 3D obliquity, ψ can be recovered using an independent measurement of the inclination of the star, i_\star . We derive an estimate of $i_\star = 75^{+11}_{-17}^\circ$ by combining measurements of the stellar radius R_\star , stellar rotation period P_{rot} , and the projected rotation $v \sin i_\star$ from the RM fit (Masuda & Winn 2020). The distribution of i_\star is broad, but there is a preference for a somewhat inclined star, where $i_\star = 90^\circ$ means the spin angular momentum vector is perpendicular to our line of sight. The combination of i_\star , λ , and orbital inclination i gives a de-projected stellar obliquity of $\psi = 23^{+15}_{-12}^\circ$, which is consistent with a prograde, low stellar obliquity orbit for 55 Cnc e.

Our detection of a Rossiter-McLaughlin effect is statistically supported. Our best fit value of $v \sin i_\star$ over its corresponding error is 4.3σ . We implement leave-one-out cross-validation to compare the RM model to the null hypothesis of no detection, i.e. a straight line (Andrae et al. 2010). This returns a χ^2 of 70.3 for an RM model vs. 86.9 for a model without RM, implying that the RM model better predicts the “unseen” left out data and is therefore the better choice of model. The Bayesian information criterion based on the maximum likelihood fit to the full data set also favors the RM model over a straight line by 8.5, where a difference greater than 6 is typically considered significant (Schwarz 1978).

We use Gaussian process (GP) regression bootstrapping to establish a false alarm probability for our measured RM effect. We generate 1000 random pairs of data samples using a GP with a Matérn-3/2 covariance function whose hyperparameters are set to reflect the noise properties of the observed EXPRES data. These data have no injected RM signal as the samples have been drawn from the prior distribution over datasets. Of these realizations, only 0.3% return a best fit RM model with a solution consistent to the RM fit with the real data, illustrated by the yellow contour in Supplementary Figure 2. Our detection therefore has a false alarm probability of 0.3%.



Supplementary Figure 2. A 2D histogram of the results from maximum likelihood RM fits to 1000 data samples using Gaussian process regression bootstrapping. The yellow contour represents the 68% credible interval of the fit to the original data. Three out of 1000 versions of the generated mock data (red dots) show signals consistent with our original data, signifying a 0.3% false positive probability. One point is outside the range of the figure at $v \sin i_\star = 4.09 \text{ km s}^{-1}$.

5. DATA AVAILABILITY

The EXPRES radial velocities used in this study are published as part of the supplementary information. The TESS data used in this study is publicly available and can be obtained from the Mikulski Archive for Space Telescopes (MAST; <https://archive.stsci.edu/missions-and-data/tess>).

6. CODE AVAILABILITY

The code associated with this work used only open source software. This research made use of `SciPy` (Virtanen et al. 2020), `NumPy` (Oliphant 2006–; van der Walt et al. 2011), `Astropy` (Astropy Collaboration et al. 2013; Price-Whelan et al. 2018), `lightkurve` (Lightkurve Collaboration et al. 2018), `starry` (Luger et al. 2019), `emcee` (Foreman-Mackey et al. 2013), `celerite` (Foreman-Mackey et al. 2017; Foreman-Mackey 2018), `ellc` (Maxted 2016), `LDTk` (Parviainen & Aigrain 2015). This research also made use of `exoplanet` (Foreman-Mackey et al. 2020) and its dependencies (Agol et al. 2020; Astropy Collaboration et al. 2013; Price-Whelan et al. 2018; Kipping 2013; Luger et al. 2019; Salvatier et al. 2016; Theano Development Team 2016).

7. ACKNOWLEDGEMENTS

We thank the anonymous referees for improving this manuscript with their thoughtful feedback. These results made use of data provided by the EXPRES team using the EXtreme PREcision Spectrograph at the Lowell Discovery telescope, Lowell Observatory. Lowell is a private, non-profit institution dedicated to astrophysical research and public appreciation of astronomy and operates the LDT in partnership with Boston University, the University of Maryland, the University of Toledo, Northern Arizona University and Yale University. EXPRES was designed and built at Yale with financial support from NSF MRI-1429365, NSF ATI-1509436 and Yale University. Research with EXPRES is possible thanks to the generous support from NSF AST-2009528, NSF 1616086, NASA 80NSSC18K0443, the Heising-Simons Foundation, and an anonymous donor in the Yale alumni community. This paper includes data collected with the TESS mission, obtained from the MAST data archive at the Space Telescope Science Institute (STScI). Funding for the TESS mission is provided by the NASA Explorer Program. STScI is operated by the Association of Universities for Research in Astronomy, Inc., under NASA contract NAS 5-26555. V.K. and J.L. acknowledge support from NSF awards AST-2009501 and AST-2009343. J.M.B. acknowledges support from NASA grants 80NSSC21K0009 and 80NSSC21K0571. R.M.R. acknowledges support from the Heising-Simons 51 Pegasi b Postdoctoral Fellowship.

8. AUTHOR CONTRIBUTIONS

L.L.Z. designed the project and drafted the manuscript. V.K. led the analysis and drafted the manuscript. S.C.M. contributed to the scientific interpretation. C.H. processed the TESS data. L.L.Z., J.M.B., J.L., A.E.S., R.M.R., S.H.C.C., S.A.W., D.A.F. are members of the EXPRES team that built and commissioned EXPRES, maintain the instrument for high precision work, and supervise the data reduction pipeline. D.A.F. is the PI of the EXPRES Team and derived the EXPRES RVs. J.M.B. ran the stellar parameter analysis. L.L.Z., V.K., J.M.B., J.L., S.H.C.C., S.A.W., and D.A.F. contributed to the EXPRES observations.

9. COMPETING INTERESTS

The authors declare no competing interests.

REFERENCES

Agol, E., Luger, R., & Foreman-Mackey, D. 2020, AJ, 159, 123, doi: [10.3847/1538-3881/ab4fee](https://doi.org/10.3847/1538-3881/ab4fee)

Albrecht, S. H., Dawson, R. I., & Winn, J. N. 2022, arXiv e-prints, arXiv:2203.05460. <https://arxiv.org/abs/2203.05460>

Andrae, R., Schulze-Hartung, T., & Melchior, P. 2010, arXiv:1012.3754 [astro-ph, physics:physics, stat]. <https://arxiv.org/abs/1012.3754>

Astropy Collaboration, Robitaille, T. P., Tollerud, E. J., et al. 2013, A&A, 558, A33, doi: [10.1051/0004-6361/201322068](https://doi.org/10.1051/0004-6361/201322068)

Blackman, R. T., Fischer, D. A., Jurgenson, C. A., et al. 2020, AJ, 159, 238, doi: [10.3847/1538-3881/ab811d](https://doi.org/10.3847/1538-3881/ab811d)

Boué, G., & Fabrycky, D. C. 2014a, ApJ, 789, 111, doi: [10.1088/0004-637X/789/2/111](https://doi.org/10.1088/0004-637X/789/2/111)

Boué, G., & Fabrycky, D. C. 2014b, in Complex Planetary Systems, Proceedings of the International Astronomical Union, Vol. 310, 62–65

Bourrier, V., & Hébrard, G. 2014, *A&A*, 569, A65, doi: [10.1051/0004-6361/201424266](https://doi.org/10.1051/0004-6361/201424266)

Bourrier, V., Dumusque, X., Dorn, C., et al. 2018, *A&A*, 619, A1, doi: [10.1051/0004-6361/201833154](https://doi.org/10.1051/0004-6361/201833154)

Bourrier, V., Lovis, C., Cretignier, M., et al. 2021, *A&A*, 654, A152, doi: [10.1051/0004-6361/202141527](https://doi.org/10.1051/0004-6361/202141527)

Brewer, J. M., Fischer, D. A., Valenti, J. A., & Piskunov, N. 2016, *ApJS*, 225, 32, doi: [10.3847/0067-0049/225/2/32](https://doi.org/10.3847/0067-0049/225/2/32)

Butler, R. P., Marcy, G. W., Williams, E., Hauser, H., & Shirts, P. 1997, *ApJL*, 474, L115, doi: [10.1086/310444](https://doi.org/10.1086/310444)

Cegla, H. M., Oshagh, M., Watson, C. A., et al. 2016, *ApJ*, 819, 67, doi: [10.3847/0004-637X/819/1/67](https://doi.org/10.3847/0004-637X/819/1/67)

Christiansen, J. L., Vanderburg, A., Burt, J., et al. 2017, *AJ*, 154, 122, doi: [10.3847/1538-3881/aa832d](https://doi.org/10.3847/1538-3881/aa832d)

Dai, F., Masuda, K., & Winn, J. N. 2018, *ApJL*, 864, L38, doi: [10.3847/2041-8213/aadd4f](https://doi.org/10.3847/2041-8213/aadd4f)

Dawson, R. I., & Fabrycky, D. C. 2010, *ApJ*, 722, 937, doi: [10.1088/0004-637X/722/1/937](https://doi.org/10.1088/0004-637X/722/1/937)

Demory, B.-O., Gillon, M., Deming, D., & Seager, S. 2011, in AAS/Division for Extreme Solar Systems Abstracts, Vol. 2, AAS/Division for Extreme Solar Systems Abstracts, 17.04

Demory, B.-O., Gillon, M., de Wit, J., et al. 2016, *Nature*, 532, 207, doi: [10.1038/nature17169](https://doi.org/10.1038/nature17169)

Fischer, D. A., Marcy, G. W., Butler, R. P., et al. 2008, *ApJ*, 675, 790, doi: [10.1086/525512](https://doi.org/10.1086/525512)

Foreman-Mackey, D. 2018, *Research Notes of the American Astronomical Society*, 2, 31, doi: [10.3847/2515-5172/aaaf6c](https://doi.org/10.3847/2515-5172/aaaf6c)

Foreman-Mackey, D., Agol, E., Ambikasaran, S., & Angus, R. 2017, *AJ*, 154, 220, doi: [10.3847/1538-3881/aa9332](https://doi.org/10.3847/1538-3881/aa9332)

Foreman-Mackey, D., Hogg, D. W., Lang, D., & Goodman, J. 2013, *PASP*, 125, 306, doi: [10.1086/670067](https://doi.org/10.1086/670067)

Foreman-Mackey, D., Luger, R., Czekala, I., et al. 2020, exoplanet-dev/exoplanet v0.4.0, doi: [10.5281/zenodo.1998447](https://doi.org/10.5281/zenodo.1998447), <https://doi.org/10.5281/zenodo.1998447>

Gelman, A., Carlin, J., Stern, H., & Rubin, D. 2003, Bayesian Data Analysis, Second Edition, Chapman & Hall/CRC Texts in Statistical Science (Taylor & Francis). <https://books.google.co.uk/books?id=TNYhbkXQSjAC>

Hansen, B. M. S., & Zink, J. 2015, *MNRAS*, 450, 4505, doi: [10.1093/mnras/stv916](https://doi.org/10.1093/mnras/stv916)

Husser, T.-O., Wende-von Berg, S., Dreizler, S., et al. 2013, *Astronomy and Astrophysics*, 553, A6, doi: [10.1051/0004-6361/201219058](https://doi.org/10.1051/0004-6361/201219058)

Jenkins, J. M. 2016, IAU Focus Meeting, 29A, 210, doi: [10.1017/S1743921316002842](https://doi.org/10.1017/S1743921316002842)

Jurgenson, C., Fischer, D., McCracken, T., et al. 2016, in *Proc. SPIE*, Vol. 9908, Ground-based and Airborne Instrumentation for Astronomy VI, 99086T

Kaib, N. A., Raymond, S. N., & Duncan, M. J. 2011, *ApJL*, 742, L24, doi: [10.1088/2041-8205/742/2/L24](https://doi.org/10.1088/2041-8205/742/2/L24)

Kipping, D., & Jansen, T. 2020, *Research Notes of the American Astronomical Society*, 4, 170, doi: [10.3847/2515-5172/abbc0f](https://doi.org/10.3847/2515-5172/abbc0f)

Kipping, D. M. 2013, *MNRAS*, 435, 2152, doi: [10.1093/mnras/stt1435](https://doi.org/10.1093/mnras/stt1435)

Kunovac Hodžić, V., Triaud, A. H. M. J., Cegla, H. M., Chaplin, W. J., & Davies, G. R. 2021, *Monthly Notices of the Royal Astronomical Society*, 502, 2893, doi: [10.1093/mnras/stab237](https://doi.org/10.1093/mnras/stab237)

Levine, S. E., Bida, T. A., Chylek, T., et al. 2012, in *Society of Photo-Optical Instrumentation Engineers (SPIE) Conference Series*, Vol. 8444, Ground-based and Airborne Telescopes IV, 844419

Liebing, F., Jeffers, S. V., Reiners, A., & Zechmeister, M. 2021, *Astronomy and Astrophysics*, 654, A168, doi: [10.1051/0004-6361/202039607](https://doi.org/10.1051/0004-6361/202039607)

Lightkurve Collaboration, Cardoso, J. V. d. M., Hedges, C., et al. 2018, Lightkurve: Kepler and TESS time series analysis in Python, *Astrophysics Source Code Library*. <http://ascl.net/1812.013>

López-Morales, M., Triaud, A. H. M. J., Rodler, F., et al. 2014, *ApJL*, 792, L31, doi: [10.1088/2041-8205/792/2/L31](https://doi.org/10.1088/2041-8205/792/2/L31)

Luger, R., Agol, E., Foreman-Mackey, D., et al. 2019, *AJ*, 157, 64, doi: [10.3847/1538-3881/aae8e5](https://doi.org/10.3847/1538-3881/aae8e5)

Marcy, G. W., Butler, R. P., Fischer, D. A., et al. 2002, *ApJ*, 581, 1375, doi: [10.1086/344298](https://doi.org/10.1086/344298)

Masuda, K., & Winn, J. N. 2020, *The Astronomical Journal*, 159, 81, doi: [10.3847/1538-3881/ab65be](https://doi.org/10.3847/1538-3881/ab65be)

Maxted, P. F. L. 2016, *Astronomy and Astrophysics*, 591, A111, doi: [10.1051/0004-6361/201628579](https://doi.org/10.1051/0004-6361/201628579)

McArthur, B. E., Endl, M., Cochran, W. D., et al. 2004, *ApJL*, 614, L81, doi: [10.1086/425561](https://doi.org/10.1086/425561)

Meunier, N., Mignon, L., & Lagrange, A. M. 2017, *A&A*, 607, A124, doi: [10.1051/0004-6361/201731017](https://doi.org/10.1051/0004-6361/201731017)

Millholland, S. C., & Spalding, C. 2020, *ApJ*, 905, 71, doi: [10.3847/1538-4357/abc4e5](https://doi.org/10.3847/1538-4357/abc4e5)

Ohta, Y., Taruya, A., & Suto, Y. 2005, *The Astrophysical Journal*, 622, 1118, doi: [10.1086/428344](https://doi.org/10.1086/428344)

Oliphant, T. 2006–, NumPy: A guide to NumPy, USA: Trelgol Publishing. <http://www.numpy.org/>

Parviainen, H., & Aigrain, S. 2015, *MNRAS*, 453, 3821, doi: [10.1093/mnras/stv1857](https://doi.org/10.1093/mnras/stv1857)

Pepe, F., Cristiani, S., Rebolo, R., et al. 2013, *The Messenger*, 153, 6

Petersburg, R. R., Ong, J. M. J., Zhao, L. L., et al. 2020, *AJ*, 159, 187, doi: [10.3847/1538-3881/ab7e31](https://doi.org/10.3847/1538-3881/ab7e31)

Petrovich, C., Deibert, E., & Wu, Y. 2019, *AJ*, 157, 180, doi: [10.3847/1538-3881/ab0e0a](https://doi.org/10.3847/1538-3881/ab0e0a)

Piskunov, N., & Valenti, J. A. 2017, *Astronomy and Astrophysics*, 597, A16, doi: [10.1051/0004-6361/201629124](https://doi.org/10.1051/0004-6361/201629124)

Price-Whelan, A. M., Sipőcz, B. M., Günther, H. M., et al. 2018, *AJ*, 156, 123, doi: [10.3847/1538-3881/aabc4f](https://doi.org/10.3847/1538-3881/aabc4f)

Pu, B., & Lai, D. 2019, *MNRAS*, 488, 3568, doi: [10.1093/mnras/stz1817](https://doi.org/10.1093/mnras/stz1817)

Salvatier, J., Wiecki, T. V., & Fonnesbeck, C. 2016, *PeerJ Computer Science*, 2, e55

Schwarz, G. 1978, *The Annals of Statistics*, 6, 461, doi: [10.1214/aos/1176344136](https://doi.org/10.1214/aos/1176344136)

Shporer, A., & Brown, T. 2011, *The Astrophysical Journal*, 733, 30, doi: [10.1088/0004-637X/733/1/30](https://doi.org/10.1088/0004-637X/733/1/30)

Steffen, J. H., & Coughlin, J. L. 2016, *Proceedings of the National Academy of Science*, 113, 12023, doi: [10.1073/pnas.1606658113](https://doi.org/10.1073/pnas.1606658113)

Theano Development Team. 2016, arXiv e-prints, abs/1605.02688

Triaud, A. H. M. J. 2018, in *Handbook of Exoplanets*, ed. H. J. Deeg & J. A. Belmonte, 2

Valenti, J. A., & Fischer, D. A. 2005, *ApJS*, 159, 141, doi: [10.1086/430500](https://doi.org/10.1086/430500)

van der Walt, S., Colbert, S. C., & Varoquaux, G. 2011, *Computing in Science Engineering*, 13, 22, doi: [10.1109/MCSE.2011.37](https://doi.org/10.1109/MCSE.2011.37)

Virtanen, P., Gommers, R., Oliphant, T. E., et al. 2020, *Nature Methods*, 17, 261, doi: <https://doi.org/10.1038/s41592-019-0686-2>

von Braun, K., Boyajian, T. S., ten Brummelaar, T. A., et al. 2011, *ApJ*, 740, 49, doi: [10.1088/0004-637X/740/1/49](https://doi.org/10.1088/0004-637X/740/1/49)

Winn, J. N., Matthews, J. M., Dawson, R. I., et al. 2011, *ApJL*, 737, L18, doi: [10.1088/2041-8205/737/1/L18](https://doi.org/10.1088/2041-8205/737/1/L18)

Zhao, L. L., Fischer, D. A., Ford, E. B., et al. 2022, *AJ*, 163, 171, doi: [10.3847/1538-3881/ac5176](https://doi.org/10.3847/1538-3881/ac5176)